Applied Surface Science 684 (2025) 161982

Contents lists available at ScienceDirect

Applied Surface Science

journal homepage: www.elsevier.com/locate/apsusc

Full Length Article

Evolution of the liquid/solid interface roughness in $Si_{1-x}Ge_x$ layers processed by nanosecond laser annealing

R. Demoulin [a,*,1], R. Daubriac [b,1], S. Kerdilès [c], L. Dagault [c], O. Adami [d], D. Ricciarelli [e], J.-M. Hartmann [c], F. Chiodi [d], A.M. Mio [e], M. Opprecht [c], E. Scheid [b], P.Acosta Alba [c], D. Débarre [d], A.La Magna [e], F. Cristiano [b]

[a] Univ Rouen Normandie, INSA Rouen Normandie, CNRS, Normandie Univ, GPM UMR 6634, F-76000 Rouen, France
[b] LAAS-CNRS, Université de Toulouse 31400 Toulouse, France
[c] Université Grenoble Alpes, CEA, LETI 38000 Grenoble, France
[d] Université Paris-Saclay, CNRS, C2N, Palaiseau, France
[e] CNR-IMM, Catania, Italy

ARTICLE INFO

Keywords:
Pulsed laser annealing
Silicon–germanium
Strain
Liquid–solid interface
Roughness

ABSTRACT

Pulsed laser annealing is a relevant alternative to conventional thermal processes for future technology nodes as it enables the application of a fast and local thermal budget. Such high-energy process can lead to the formation of a liquid phase that recrystallizes upon heat dissipation, through a high velocity liquid/solid interface moving towards the surface. Here, we report on the evolution of the liquid/solid interface roughness and its influence on the crystallinity of $Si_{1-x}Ge_x$ layers depending on multiple parameters (strain state, doping level, Ge content, and pulse duration). This has been conducted with a roughness quantification method based on cross-section STEM-HAADF micrographs. It has been established that the liquid/solid roughness can be decreased by: (i) a compressive strain decrease, (ii) the use of short duration laser pulses or (iii) a reduction of the initial Ge content. The Ge content and strain must correspond to suitable values for optimized MOSFET performances. Consequently, strain and pulse duration were found to be pertinent levers for liquid/solid interface roughness reduction. Increasing the amount of boron atoms in s-$Si_{1-x}Ge_x$:B/Si systems is another relevant strategy, as compressive strain decrease would then be associated with a beneficial contact resistance lowering in the source-drain regions of p-type MOSFET devices.

1. Introduction

$Si_{1-x}Ge_x$ alloys took a major place in the microelectronic industry because of their potential for MOSFETs devices. These last decades, continuous miniaturization of these electronic devices yielded higher performances. Now, research on new 3D-based architectures is actively engaged. However, new issues were highlighted concerning the use of conventional Rapid Thermal Annealing essentially for the fabrication of ultra-shallow junctions and innovative 3D devices. Ultra-Violet Nanosecond Laser Annealing (UV-NLA) has attracted considerable attention thanks to its low and localised thermal budget [1–3]. Indeed, UV-NLA can be used to perform high temperature annealing at the surface while keeping the underlying material at lower temperature [4,5]. It has also been evidenced that UV-NLA enables to reach dopant concentrations much higher than their solubility limits in Si or Ge by reaching the melt regime [6–8]. Consequently, this processing method should pave the way to the diversification of device architectures with the introduction of 3D schemes, and to a general improvement of device performances [9–11].

Laser annealing in the melt regime on Si, Ge and $Si_{1-x}Ge_x$ alloys has been studied for years [3,12–14]. Most of these studies have focused on the surface structuring induced by such annealing. In $Si_{1-x}Ge_x$ alloys, segregation-induced self-organization has been identified. Samples exposed to laser annealing may exhibit nano-islands [15,16], ripples [17,18] or cellular [19] Ge-enriched structures at their surface depending on layer characteristics and annealing conditions (Ge content, layer thickness, solidification velocity, and so on). This type of surface self-organization was explained based on the evolution of the

* Corresponding author.
E-mail address: remi.demoulin1@univ-rouen.fr (R. Demoulin).
[1] These two authors contributed equally to this work.

https://doi.org/10.1016/j.apsusc.2024.161982
Received 13 September 2024; Received in revised form 8 November 2024; Accepted 29 November 2024
Available online 1 December 2024

liquid/solid (l/s) interface (corresponding to the melting front) during layer recrystallization. In particular, based on Mullins-Sekerka perturbation theory, Weizman et al. proposed that the self-organization of Ge-enriched islands and ripples was due to the instability of the planar l/s interface during recrystallization [16]. This instability growth regime mainly depends on the Ge content and the solidification velocity. Narayan et al. have used a similar model to explain the segregation of solute atoms in indium-implanted Si resulting in the formation of a cellular morphology [20]. In $Si_{1-x}Ge_x$ layers, the formation of the cellular morphology originates from Ge segregation, which was confirmed by energy-dispersive X-ray (EDX) experiments [21]. However, only a few experimental investigations were carried out on the direct characterization of this l/s interface, from which all of these specific structuring likely arise [22,23]. To get a better understanding of the melting and solidification processes, deeper investigations on this l/s interface are definitely needed.

In previous papers, we have investigated the impact of UV-NLA on 30 nm-thick strained $Si_{1-x}Ge_x$ layers [15,22]. In these layers, the different melt regimes (from sub-melt to full melt) and their repercussions on layer crystallinity were described. In particular, these investigations highlighted a strong correlation between the l/s interface roughness and the strain state of $Si_{1-x}Ge_x$ layers. This was explained based on the elastic energy stored in $Si_{1-x}Ge_x$ layers. Two cases were distinguished. First, when the l/s interface was smooth, i.e. for an elastic energy lower than a critical value of around 750 mJ cm^{-2}, the $Si_{1-x}Ge_x$ layer remained perfectly strained after recrystallization. Second, when the l/s interface exhibited some roughness, the recrystallization systematically resulted in the formation of strain relieving defects. In that case, $Si_{1-x}Ge_x$ layers relaxed even if the stored elastic energy was lower than that critical value. At this point, more investigations were required to better understand and ideally control the evolution of this roughness, in order to avoid layer relaxation.

In the present paper, we carried out a quantitative study of the evolution of the l/s interface roughness as a function of several experimental parameters, such as the strain state of the $Si_{1-x}Ge_x$ layer, the doping level or the Ge content. The objective was threefold: (i) improve our understanding of the origin of the l/s interface roughness, (ii) understand its impact on the crystallinity of $Si_{1-x}Ge_x$ layers and (iii) identify the best process conditions yielding fully strained and defect-free layers after UV-NLA in the melt regime.

2. Materials and methods

2.1. Elaboration and processing of $Si_{1-x}Ge_x$ layers

Three different series of $Si_{1-x}Ge_x$ layers were investigated in this work. Specific characteristics and processing methods used on these layers are listed in Table 1. Undoped and in-situ boron-doped 30 nm-thick strained $Si_{1-x}Ge_x$ layers (x = 0.1 – 0.4) were grown at 20 Torr on 300 mm n-type Si (001) wafers by Reduced Pressure Chemical Vapor Deposition (RPCVD) in an Epsilon 3200 tool from ASM. These strained layers are referred to, in the following, as s-$Si_{1-x}Ge_x$ and s-$Si_{1-x}Ge_x$:B. Before the deposition, a "HF-last" wet cleaning followed by an in-situ H_2 bake at 1100 °C were performed on Si surfaces. The undoped series of strained $Si_{1-x}Ge_x$ layers has already been used in our previous investigations [15].

Si_2H_6 and GeH_4 were used as Si and Ge gaseous precursors for the 550 °C growth of the intrinsic s-$Si_{1-x}Ge_x$ layers. Meanwhile, SiH_2Cl_2, GeH_4 and B_2H_6 were used as Si, Ge and B gaseous precursors for the 650 °C epitaxy of s-$Si_{1-x}Ge_x$:B layers. In that case, $Si_{1-x}Ge_x$:B growth was preceded by the deposition of 100 nm thick n-type doped Si layers to form a p-n junction. Three levels of B doping were considered, at 7.4×10^{19}, 1.4×10^{20} and 2.3×10^{20} at.cm^{-3} (as measured by Secondary Ions Mass Spectrometry).

Thick and fully relaxed $Si_{1-x}Ge_x$ layers (x = 0.2 and 0.5) were otherwise grown, at 20 Torr, on 200 mm p-type Si (001) substrates. These layers are referred to, in the following, as r-$Si_{1-x}Ge_x$. The fabrication was carried out by RPCVD, in an Epi Centura 5200 tool, following a two steps process: (i) a deposition of a $Si_{1-x}Ge_x$ layer with linearly graded Ge concentration, with a 10 % μm^{-1} ramp used to reach the targeted Ge concentration, followed by (ii) a deposition of about one-micron thick constant composition $Si_{0.8}Ge_{0.2}$ or $Si_{0.5}Ge_{0.5}$ layers. They were grown at 850–900 °C to promote the glide of misfit dislocations and minimize the threading dislocation density, resulting in the formation of strain-free micron-thick r-$Si_{1-x}Ge_x$ layers on the top. Finally, Chemical Mechanical Polishing was performed on layers to remove the surface cross-hatch patterns inherent to such stacks [24].

Concerning the laser annealing, all three series of $Si_{1-x}Ge_x$ layers were annealed by UV-NLA. This was performed in a SCREEN LT-3100 system based on a XeCl excimer laser with a 308 nm wavelength, a pulse duration of 146 ns or 160 ns and a pulse frequency of 4 Hz. The laser beam is square-shaped (15×15 μm^2) with a uniformity below 2 %. Annealing were performed under N_2 ambient. A second set of s-$Si_{0.7}Ge_{0.3}$:B (7.4×10^{19} at.cm^{-3}) layers were annealed in a Pulsed Laser Induced Epitaxy system based on a XeCl excimer laser with a 308 nm wavelength, a pulse duration of 25 ns and a pulse frequency of 2 Hz, under ultrahigh vacuum (10^{-9} mbar). The laser beam is square-shaped (3×3 μm^2) with a uniformity around 1.5 %. In both cases, the range of laser energy densities (ED) was selected in order to investigate the evolution of $Si_{1-x}Ge_x$ layers in the various laser regimes. Indeed, laser annealing of $Si_{1-x}Ge_x$ layers can be divided in three steps: *(i)* the surface melt, corresponding to the emergence of melted areas at the layer surface, *(ii)* the partial melt, for which a continuous melted layer is formed at the surface of $Si_{1-x}Ge_x$ layer and *(iii)* the full melt, corresponding to the complete melting of the $Si_{1-x}Ge_x$ layer [11].

Table 1
Characteristics of $Si_{1-x}Ge_x$ layers used in this study, with their respective laser annealing conditions (pulse duration, wavelength, surface melt and partial melt threshold).

Series	Ge content (%)	Thickness (nm)	Doping (cm^{-3})	UV-NLA	Surface melt threshold (J cm^{-2})	Partial melt threshold (J cm^{-2})
s-SiGe	10	30	–	146 ns 308 nm	1.66	1.94
	20	30	–		1.55	1.86
	30	30	–		1.45	1.75
	40	30	–		1.32	1.72
s-SiGe:B	30	30	(Low) 7.4×10^{19}	25 ns 308 nm	n/a	0.600*
	30	30	(Low) 7.4×10^{19}	160 ns 308 nm	1.46	1.78
	30	30	(Medium) 1.4×10^{20}		1.45	1.78
	30	30	(High) 2.3×10^{20}		1.48	1.78
r-SiGe	20	1000	–	160 ns 308 nm	0.650	0.800
	50	1000	–		0.525	0.650

* For 25 ns UV-NLA, partial melt threshold corresponds to an estimation based on TEM observations.

2.2. Structural characterization of $Si_{1-x}Ge_x$ layers

The evolution of the l/s interface in the melt regimes was investigated in all three series thanks to cross-sectional Transmission Electron Microscopy (TEM). TEM investigations were mainly carried out by Scanning TEM in high Annular Dark Field (STEM-HAADF) mode and by Energy Dispersive X-ray spectroscopy (STEM-EDX), while the presence of defects in $Si_{1-x}Ge_x$ layers was studied by Weak-Beam Dark-Field TEM (WBDF-TEM). JEOL JEM-2100F and JEOL JEM-ARM200F Cold FEG microscopes were used for the current study. TEM lamellas were prepared using a dual beam Helios Nanolab 600i FIB-SEM.

Additional information on the strain state and on the crystallinity of the $Si_{1-x}Ge_x$ layers were obtained by High-resolution X-ray Diffraction (HR-XRD). For HR-XRD, Reciprocal Space Maps (RSM) were acquired around the (224) reflection with an X'pert Pro PANalytical tool. RSMs were used to estimate the degree of strain relaxation for laser annealed samples.

2.3. Method for the quantification of l/s interface roughness

The contrast observed on STEM-HAADF micrographs is directly related to the chemical composition, the measured intensity increasing with the atomic number. This enables to differentiate phases in laser annealed $Si_{1-x}Ge_x$ layers. It is known that, in the melt regime, UV-NLA of $Si_{1-x}Ge_x$ layers induces a redistribution of Ge toward the surface [15,25]. Fig. 1 a-b shows two STEM-HAADF micrographs recorded in 30 nm-thick s-$Si_{1-x}Ge_x$:B layers annealed by UV-NLA. In the melted area, the redistribution of Ge is characterized by a depletion of Ge content near to the l/s interface and an increase of Ge content at the surface. In the STEM-HAADF mode, the redistribution of Ge is marked by a contrast gradient in the annealed area. This imaging technique also allows to evidence the position and the shape of the l/s interface, which corresponds to the limit between melted and un-melted areas. In these micrographs, an intensity threshold (along the *z*-axis) is determined at each *x*-coordinate to extract the depth (i.e. the *y*-position) of the l/s interface. In the partial melt regime (i.e. when the melt depth is lower than the $Si_{1-x}Ge_x$ layer thickness), this threshold corresponds to the mid-level between the lowest intensity of melted area and the highest intensity of unmelted area. The correspondence of the intensity threshold is represented on Fig. 1.c. The same procedure is used for the full melt regime criterion (but with inverted contrast levels). Once the l/s interface is entirely reconstructed, the roughness *R* of the interface can be estimated using the following equation *(1)*:

$$R = \frac{1}{N}\sum_{i=1}^{n} |y_i - d_{l/s}| \quad (1)$$

The mean depth of the l/s interface is represented by $d_{l/s}$ while its depth at position *i* is given by the coordinate y_i. *N* corresponds to the total number of measurements (i.e number of pixels along the *x*-axis). Here, *R* represents the mean variation of the l/s interface around its mean depth. Using a resolution of 1024x1024 pixels, a minimum of 150 nm long STEM-HAADF micrographs are required to observe the stabilization of the R parameter. To ensure the reliability of the results, STEM-HAADF micrographs has been systematically taken in a window of 200 x 200 nm^2 to a maximum of 400 x 400 nm^2 for the calculation of the R parameter. Roughness extraction examples from STEM-HAADF micrographs are shown in Fig. 1 for (a) "rough" and (b) "flat" l/s interfaces. The l/s interfacial roughness were estimated at 1.23 ± 0.15 nm and 0.40 ± 0.09 nm, respectively. This procedure will be subsequently used in order to quantify the evolution of the roughness of the l/s interface as a function of layer parameters and processing methods.

3. Results & discussion

3.1. Evolution of the l/s interface in strained layers

3.1.1. Qualitative evolution of the l/s interface

Fig. 2 shows the evolution of a 30 nm-thick s-$Si_{0.6}Ge_{0.4}$ layer for different laser annealing conditions. By increasing the laser ED from 1.6 $J.cm^{-2}$ to 2.2 $J.cm^{-2}$, different melt regimes are encountered. The first regime corresponds to the surface melt. In fact, at 1.6 $J.cm^{-2}$, TEM micrographs evidence a localised melt resulting in the formation of isolated melted islands in-homogeneously distributed on the surface. Here, it is not possible to clearly define a l/s interface roughness as large parts of the s-$Si_{0.6}Ge_{0.4}$ surface remain un-melted. However, formation of such structures at the layer surface in the surface melt regime may certainly contribute to the formation of a rough l/s interface after the transition to the partial melt regime. This partial melt regime observed at 1.8 $J.cm^{-2}$ corresponds to the formation of a continuous liquid layer

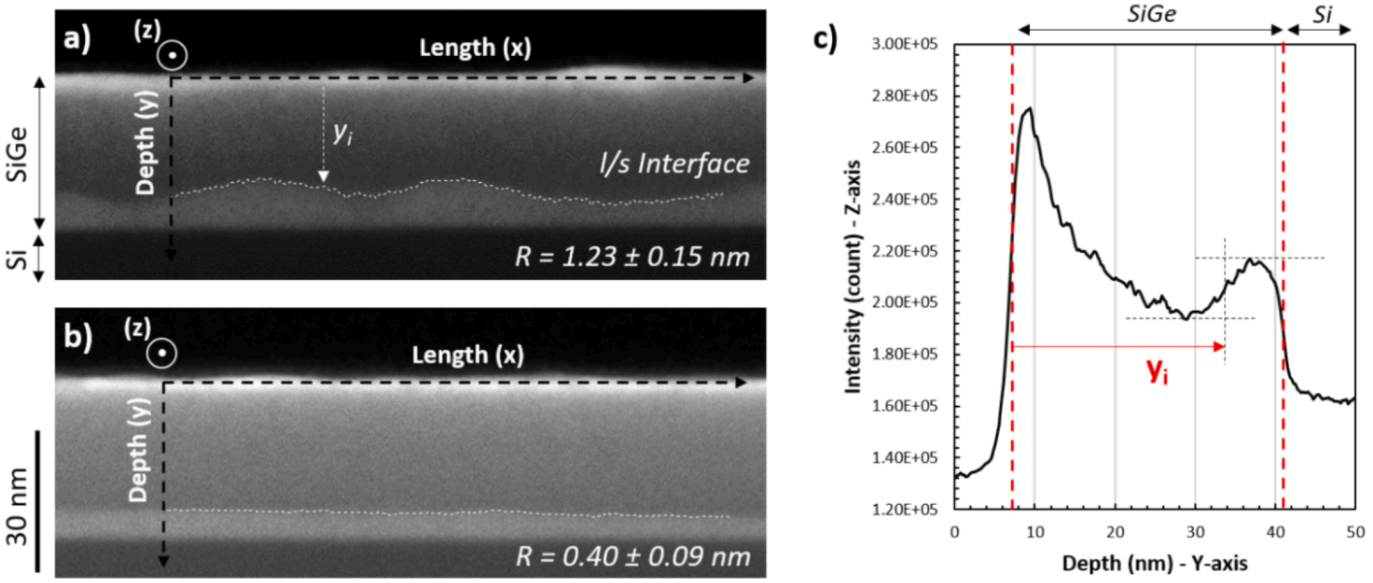

Fig. 1. Typical STEM-HAADF micrographs of laser annealed $Si_{1-x}Ge_x$. Micrographs have been taken on low (a) and high (b) doped s-$Si_{0.7}Ge_{0.3}$:B layers at an ED of 1.95 J/cm^2. Both have been overlaid with the representative curve of the l/s interface. Z-axis corresponds to the intensity. (a) and (b) show rough and flat interfaces, respectively. (c) Single intensity profile taken along the y-direction.

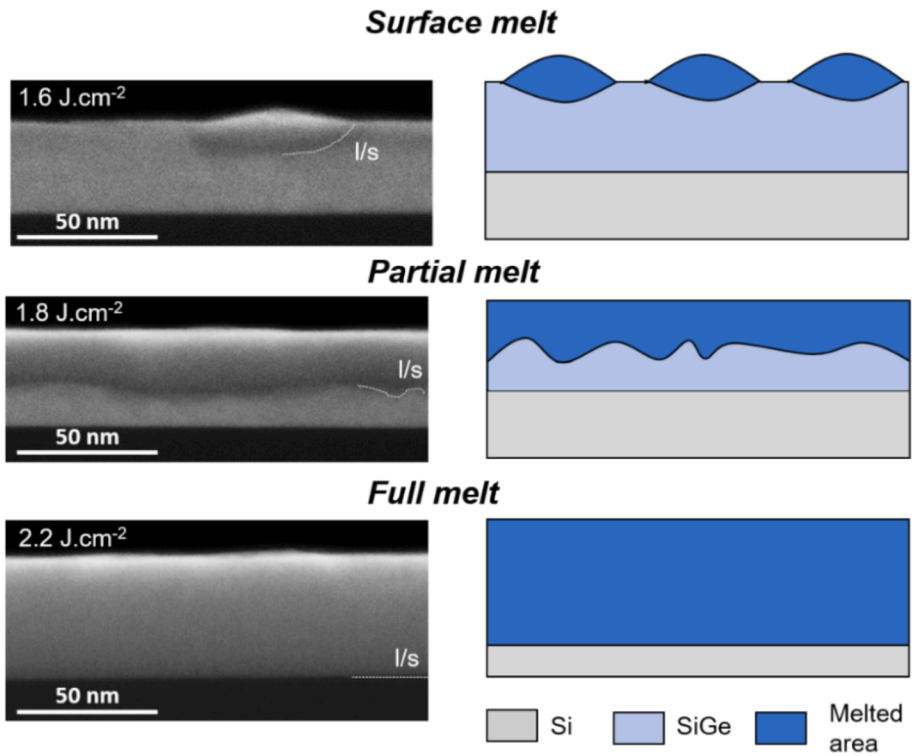

Fig. 2. STEM-HAADF micrographs of 30 nm-thick s-$Si_{0.6}Ge_{0.4}$ layers as a function of the laser ED (left). Schematization of each step of the melt process (right).

at the surface before its recrystallization. In this regime, the formation of a rough l/s interface is clearly observed. The last regime is called the full melt (i.e. the full melting of a $Si_{1-x}Ge_x$ layer sitting on a Si substrate) and can be observed for a laser ED of 2.2 $J.cm^{-2}$. When the transition from partial to full melt happens, the l/s roughness clearly decreases. This flattening can be explained by the melting temperature (T_{melt}) differences between Si (1412 °C) and Ge (938 °C). As the $Si_{1-x}Ge_x$ alloy's T_{melt} is lower than that of the Si substrate, the $Si_{1-x}Ge_x$ layer will be completely melted well before the Si substrate starts to melt. The l/s roughness thus remains very low in the full melt regime and seems to stop varying whatever the melt depth above the $Si/Si_{1-x}Ge_x$ interface. In fact, the laser annealing of the free surface leads to a heterogenous nucleation during the first melting steps, however the less defective $Si/Si_{1-x}Ge_x$ interface buried beneath the surface allow preserving the lower roughness induced by the difference of T_{melt}. Another set of laser anneals were performed on a 45 nm-thick s-$Si_{0.7}Ge_{0.3}$ layer. In this thicker layer, the l/s interface remained rough at a melt depth above 30 nm (see supporting information S1). This confirmed that the l/s interface did not progressively flatten by increasing the melt depth but instead because the $Si/Si_{1-x}Ge_x$ interface was reached by the melt front.

3.1.2. *Quantification of the l/s roughness*

Fig. 3(a) shows the link between the mean melt depths and the laser ED for Ge contents varying from 10 % to 40 % in 30 nm thick SiGe layers. Melt depths increases almost linearly with the ED, with similar slopes whatever the Ge content. This likely indicates that the melting velocity is independent of the Ge content. The ED shift to lower values for higher Ge contents is due to the lower T_{melt} of high Ge content layers. Once definitely in the full melt regime, at 2.2 $J.cm^{-2}$, all samples present a comparable melt depth (around 40–44 nm). This is related to the

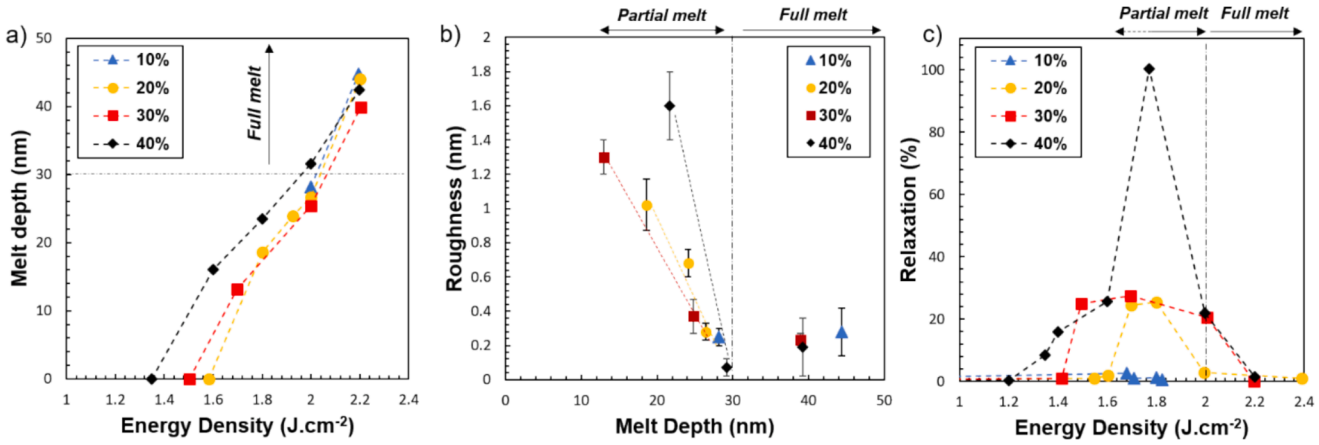

Fig. 3. (a) Evolution of the melt depth as a function of the laser ED. (b) Overview of the l/s interface roughness in various Ge content s-$Si_{1-x}Ge_x$ layers, laser-annealed in the partial and full melt. (c) Evolution of the degree of strain relaxation, from XRD, as a function of the laser ED. The Ge content varies from 10 to 40 %. The melt depth corresponds to the mean depth of the l/s interface.

definite impact of the Si substrate on the melt process.

Based on the procedure described in the section 2.3, the roughness parameters *R* of all analysed s-$Si_{1-x}Ge_x$ samples were computed as functions of melt depth, for Ge contents in the 10–40 % range. These measurements are summarized in Fig. 3(b). A similar behaviour is found for all Ge contents. For lower melt depths, a high l/s roughness is measured. This roughness decreases until the full melt regime (i.e. the Si substrate) is reached at ≃30 nm then stabilizes at a low level. The presence of such l/s roughness is correlated to the strain relaxation in s-$Si_{1-x}Ge_x$ layers. Fig. 3(c) evidences that for Ge contents of 20 to 40 %, surface and partial melt systematically lead to partial and, for 40 % of Ge and a specific ED, to full relaxation of the s-$Si_{1-x}Ge_x$ layers. The ED range over which the strain is partially relaxed otherwise increases as the Ge content increases. However, the full melt regime, with the flattest l/s interface, yields the same compressive strain state than the as-grown one (i.e. no measurable strain relaxation). It has been established that strain relaxation is directed by the elastic energy stored in the s-$Si_{1-x}Ge_x$ layer [15]. In the partial melt regime, the l/s interface roughness seems to increase for the higher Ge content. The effect of the Ge content may be due to two different mechanisms. First, the increased elastic energy induced by higher Ge contents can increase the l/s roughness. Second, an increase of the islands density and of their melt depth in the surface melt regime might result in an increased l/s roughness.

To determine the optimal working condition avoiding the formation of defects in the $Si_{1-x}Ge_x$ layer it is essential to understand the origin of the l/s interface roughness. From these preliminary experiments, we can conclude that this roughness is linked to multiple parameters such as: *(i)* the initial strain, *(ii)* the actual Ge content, and *(iii)* the nano-structuring during the surface melt. Needless to say, all these phenomena interact with each other in these sample series. To explain the origin of the l/s interface and understand its influence on the crystallinity of $Si_{1-x}Ge_x$ layers, we thus tried to decorrelate these phenomena by isolating each of them. We first reduced the initial compressive strain by high B doping at a fixed Ge content. We otherwise varied the Ge content in fully plastically relaxed, thick $Si_{1-x}Ge_x$ layers. Finally, we changed the laser pulse duration at a given Ge content. The resulting data are discussed in the following.

3.2. Effect of the initial strain state

The introduction of large amounts of small size boron atoms in a $Si_{1-x}Ge_x$ crystal lattice results, for a given Ge content, in a lattice parameter reduction of the B-doped layer compared to the un-doped one (a_B = 3.852 Å, to be compared with a_{Si} = 5.431 Å and a_{Ge} = 5.658 Å), leading in a decrease of the built-in compressive strain in s-$Si_{1-x}Ge_x$:B layers [26,27].

Ge content variations in $Si_{1-x}Ge_x$ layers can lead to a strong modification of the surface self-organization in the surface melt regime. In these layers, at the melt onset, the surface structures change from large square-shaped islands for 10 % of Ge to smaller cross-shaped islands extended in the <100> directions for 40 % of Ge [15]. Such changes may impact the evolution of the l/s interfacial roughness at the transition from surface to partial melt. To remove this "Ge content" effect, investigations were thus carried out on s-$Si_{1-x}Ge_x$:B layers with a fixed Ge content of 30 %. This enabled us to progressively reduce the built-in compressive strain by increasing B doping without interacting with the surface structuring. Three boron doping levels were analysed and estimated: 7.4×10^{19}, 1.4×10^{20} and 2.3×10^{20} at. cm^{-2} These B-doping levels are referred to, in the following, as: low, medium and high, respectively. B-doping has no influence on the laser annealing process. Indeed, surface melt and partial melt thresholds are reached for the same energy densities for un-doped and B-doped layers (Table 1). This is confirmed in Fig. 4, which shows that, at the partial melt threshold (ED = 1.78 J cm^{-2}, please refer to Table 1), the melt depth remains equivalent (≃18 nm) regardless of the B-doping level. Moreover, SEM micrographs evidences that nano-structuring on the surface is similar, confirming that a modification of the surface melt process upon in-situ B doping is not expected. However, STEM-HAADF micrographs in Fig. 1 evidenced a significant impact of B-doping on the l/s interface roughness itself.

The roughness of the l/s interface has been calculated as a function of the B-doping level for a laser ED of 1.95 J cm^{-2}, e.g. for a laser annealing in the partial melt regime (Fig. 5(a)). The corresponding STEM-HAADF micrographs are presented on Fig. 1.a-b concerning the low and high B doping, respectively. Whatever the B-doping level, melt depths were estimated around 25 nm. For the low-doped s-$Si_{0.7}Ge_{0.3}$:B layer, the l/s interface roughness was estimated around 1.2 nm. Computed *R* parameters evidenced a significant flattening of the l/s interface as the B

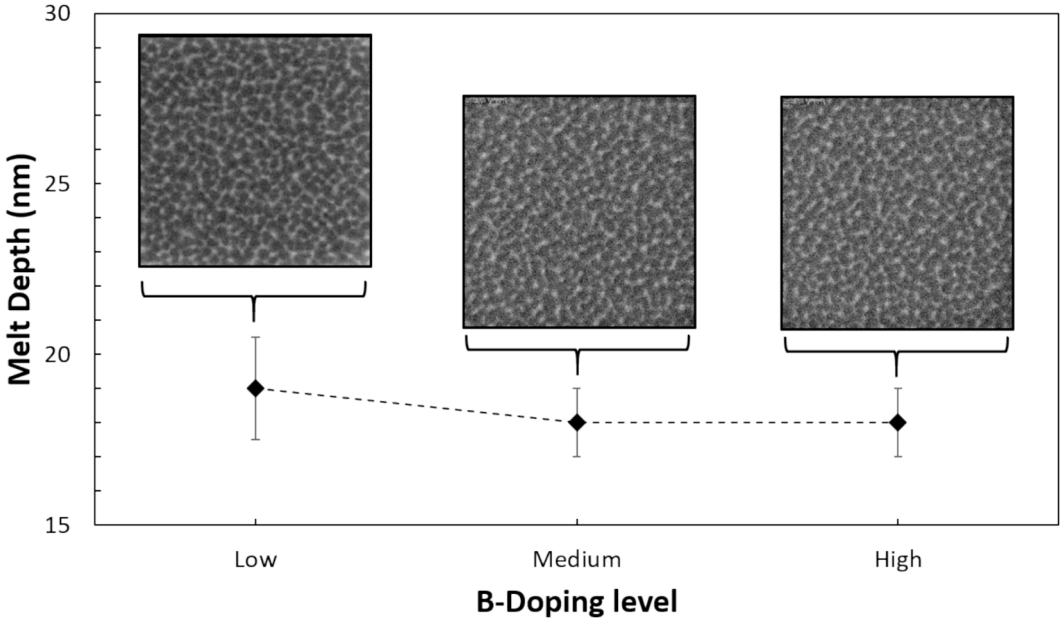

Fig. 4. Evolution of the melt depth at the partial melt threshold (for an ED of 1.78 J cm^{-2}) as a function of the B-doping level of s-$Si_{0.7}Ge_{0.3}$:B. Figure inserts: 1 × 1 μm^2 top-view SEM micrographs of the surfaces.

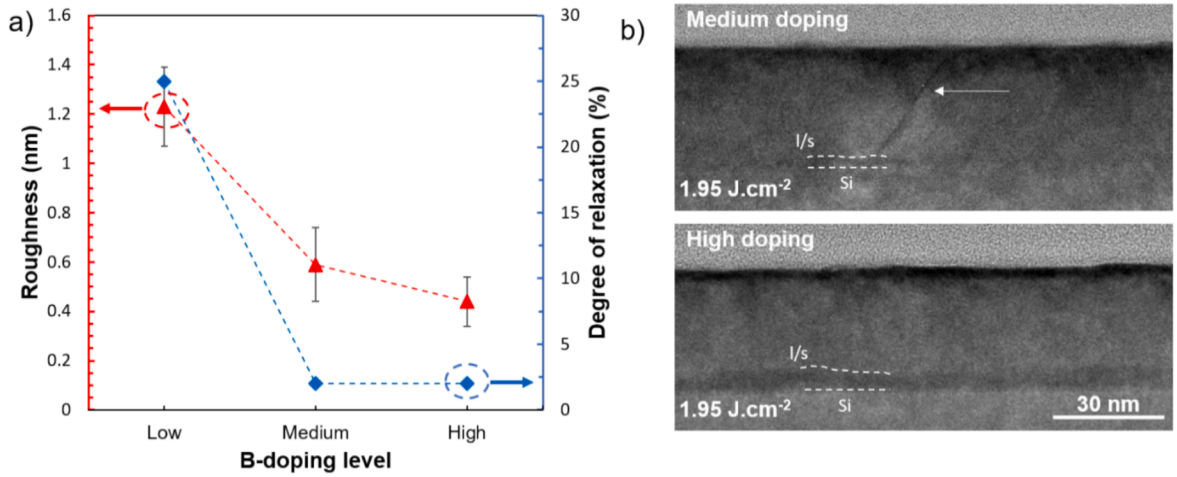

Fig. 5. (a) Evolution of the l/s interfacial roughness and degree of strain relaxation with the B-doping level and (b) Cross-sectional TEM micrographs of s-$Si_{0.7}Ge_{0.3}$:B layers annealed at ED = 1.95 J cm^{-2}.

doping increased, down to 0.5 nm for the high doping. This suggests that a decrease of the initial compressive strain in s-$Si_{1-x}Ge_x$ layers thus resulted, at least for 30 % of Ge, in a decrease of the l/s interfacial roughness.

To quantify the impact of B-doping, and so of the l/s roughness, on layer crystallinity, degrees of relaxation of these s-$Si_{0.7}Ge_{0.3}$:B layers were also extracted from HR-XRD Reciprocal Space Maps. They are shown as a function of the B-doping level in Fig. 5(a). For the low-doped sample, the s-$Si_{0.7}Ge_{0.3}$:B layer is partially relaxed (25 %) and strain relieving defects are present in the layer. For medium and high-doped samples, with smoother l/s interfaces (R < 0.6 nm), $Si_{0.7}Ge_{0.3}$:B layers remain perfectly strained. From these HR-XRD experiments, a modification of the crystalline structure of the s-$Si_{0.7}Ge_{0.3}$:B layer is observed and can be divided in two steps depending on the *R* parameter. For low B doping, the presence of a rough l/s interface thus favours the plastic relaxation of the $Si_{0.7}Ge_{0.3}$:B layer, with the formation of strain relieving defects. For higher B doping, the flat l/s interface preserves the as-grown compressive strain and the s-$Si_{0.7}Ge_{0.3}$:B layer remains defect-free. For a medium B doping, the l/s interface is smooth enough to keep the original strain state. However, punctual defects are observed in the annealed layer (Fig. 5b). Thereby, in s-$Si_{0.7}Ge_{0.3}$:B layers, an increase of the l/s interface roughness results in the formation of defects, and the accumulation of these defects leads to the relaxation of the s-$Si_{1-x}Ge_x$:B layer.

3.3. Impact of the Ge content

3.3.1. Evolution of the l/s interface roughness

As seen in the previous section, variations of the initial strain state lead to a significant modification of the l/s roughness. To decorrelate the impact of the initial strain from that of the Ge content, further investigations were carried out on fully relaxed, thick $Si_{1-x}Ge_x$ layers, with 20 % and 50 % of Ge.

STEM-HAADF cross-sections of r-$Si_{0.8}Ge_{0.2}$ are displayed in Fig. 6(a-c). In r-$Si_{1-x}Ge_x$ layers, the melting process follows the same steps than in s-$Si_{1-x}Ge_x$ layers (Fig. 2). However, the laser ED required to reach the melt threshold in r-$Si_{0.8}Ge_{0.2}$ (0.65 J cm^{-2}) is much lower than in s-$Si_{0.8}Ge_{0.2}$ (1.55 J cm^{-2}). This is due to the much lower thermal conductivity of $Si_{1-x}Ge_x$ alloys compared to Si [28], and the much larger

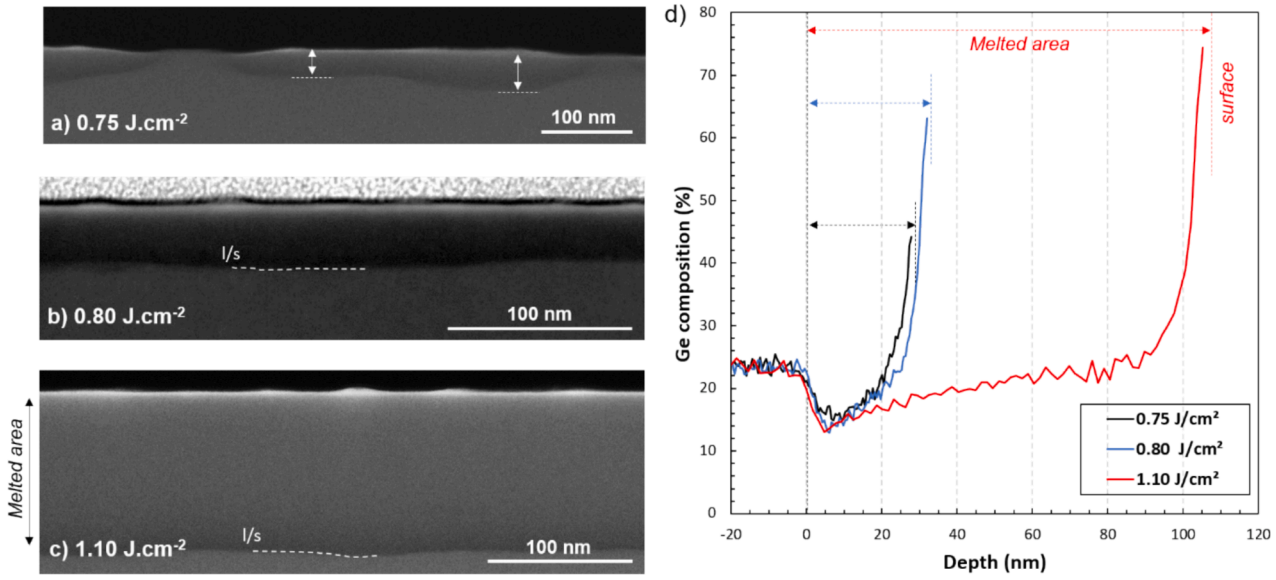

Fig. 6. Micrographs of r-$Si_{0.8}Ge_{0.2}$ layers laser annealed with ED ranging from 0.75 to 1.1 J cm^{-2} taken in the STEM-HAADF mode. (a) At 0.75 J cm^{-2}, the micrograph corresponds to the end of the surface melt regime. (b-c) For laser ED higher than 0.8 J cm^{-2}, the partial melt regime is reached. (d) Corresponding STEM-EDX Ge depth profiles. At 0.75 J cm^{-2}, the profile has been recorded in a melted area only. Zero corresponds to the l/s interface position.

thickness of the r-$Si_{1-x}Ge_x$ samples (combining a relaxed layer of 1 μm and a thick graded buffer of 2–5 μm). Here, the surface melt regime occurs for laser ED ranging from 0.65 to 0.80 J cm^{-2}. In this range, the surface islands will progressively cover the entire surface until 0.80 J cm^{-2} at which point a continuous melted layer is formed on the surface (Fig. 6(b)), evidencing a transition to the partial melt regime. Moreover, as for s-$Si_{1-x}Ge_x$ layers, the Z-contrast gradient in STEM-HAADF micrographs as well as the EDX Ge profiles presented in Fig. 6(d) highlight a Ge redistribution toward the surface inside melted areas. Concerning the l/s interface, strong variations of the melt depth already appear in the surface structuring at 0.75 J cm^{-2} in STEM-HAADF micrographs. Indeed, as shown in Fig. 6(a), the melt depth can vary from 28 up to 44 nm in a single surface island. This likely alters the evolution of the l/s interface during the transition from surface to partial melt, explaining the presence of a rough l/s interface (R = 1.2 nm) at the partial melt threshold (0.8 J cm^{-2}).

The l/s roughness is plotted as a function of melt depth in Fig. 7(a). It remains almost constant regardless of the melt depth in r-$Si_{0.8}Ge_{0.2}$. Even if this roughness is similar to that measured in low doped s-$Si_{0.7}Ge_{0.3}$:B in the partial melt regime (Fig. 5(a)), it must be noted that, in r-$Si_{0.8}Ge_{0.2}$, this l/s roughness does not induce the formation of defects in the whole layer. This means that the presence of defects in laser-annealed $Si_{1-x}Ge_x$ layers is due to both roughness and initial compressive strain. For higher Ge contents (i.e. r-$Si_{0.5}Ge_{0.5}$), the l/s interface roughness drastically increases, reaching values close to 4 nm, with once again no clear melt depth impact. In $Si_{1-x}Ge_x$ alloys, due to T_{melt} differences between Si and Ge, an increase of the Ge content induces a decrease of the T_{melt} of the alloy, and so a decrease of the melt ED threshold. Fig. 7(b) displays the evolution of the melt depth as a function of the laser ED for both layers. This T_{melt} difference always leads to deeper melt depths in r-$Si_{0.5}Ge_{0.5}$ compared to r-$Si_{0.8}Ge_{0.2}$ at fixed laser ED. Deeper melt depths during surface melt regime may thus generate higher l/s interface roughness during the transition from surface to partial melt regime. It must be noted that, even in the surface melt regime, melt depths in r-$Si_{0.8}Ge_{0.2}$ layers can exceed the thickness of our strained layers, i.e. 30 nm (Fig. 6(b)). This melt depth difference between thin, strained and thick, relaxed $Si_{1-x}Ge_x$ layers can be attributed to thermal conductivity differences. Interestingly, in semiconductors like Si, this physical parameter is weakly impacted by strain, whether compressive or tensile. Moreover, if compressive strain may be the origin of thermal conductivity variations in our study, the impact should have been the opposite, with an increase of the melt depth [29–31]. The melt depth changes are thus mainly due to considerable thickness differences [32], and, to a lesser extent, to the presence of dopants [33–35].

3.3.2. *Formation of buried Ge-rich walls inducing a cellular surface morphology*

In these layers, if no changes on the l/s interface roughness were highlighted depending on the laser ED, the self-organization of the regrown layer seems to be strongly impacted. Fig. 8 top-view SEM micrographs of the surfaces show its evolution for ED varying from 0.8 to 2.0 J cm^{-2}. At the partial melt threshold (0.8 J cm^{-2}), the surface structuring looks qualitatively the same as the one previously observed in B-doped s-$Si_{0.7}Ge_{0.3}$ layers (Fig. 4). However, at higher ED, it progressively reorganizes to stabilize in the form of a cellular morphology from 1.5 J cm^{-2}. There is then a network of regular square shaped cells with sides mainly elongated along the <110> directions, and ranging from 110 to 180 nm.

In addition to this surface self-organization, STEM-HAADF micrograph of r-$Si_{0.8}Ge_{0.2}$ layer annealed at 1.5 J cm^{-2} (Fig. 9(a)) evidenced an abrupt modification of the melted layer compared to that underneath. Bright contrasts in STEM-HAADF micrograph highlights a significant Ge segregation, with the formation of 80 nm-long Ge-rich pillars at the surface of the r-$Si_{0.8}Ge_{0.2}$ layer. These pillars correspond to the walls defining the cellular morphology on the surface. The composition of those pillars has been determined by EDX analysis (see supporting information S2). A Ge content varying from ~70 % up to ~90 % was evidenced. Given the thickness of the TEM lamella and the random disposition of cells, a superimposition of Ge-rich walls with the surrounding matrix may artificially reduce the real Ge composition during EDX analysis. Actually, these walls might be made of almost pure Ge. This evolution is not specific to r-$Si_{1-x}Ge_x$ layers and such a kind of cellular morphology has already been observed after the laser-annealing of amorphous or strained $Si_{1-x}Ge_x$ layers [19,21,36,37]. It was shown that the layer thickness and the Ge content could alter the features of this self-organization [21].

A model explaining the formation of a cellular morphology in laser-annealed $Si_{1-x}Ge_x$ was proposed in the literature, based on the analysis of Cz-grown $Si_{0.85}Ge_{0.15}$ layers [23,38]. In these experiments, the l/s interface switched from planar to faceted in the <110> directions. This faceting generated a lateral segregation of Ge and the growth of Ge-rich or pure Ge phases in valleys, reducing the growth velocity at these locations. This growth velocity difference between Ge-rich and Ge-poor regions then led to the formation of Ge-rich walls up to the layer surface. In the present case, independently of the Ge content, the initial l/s

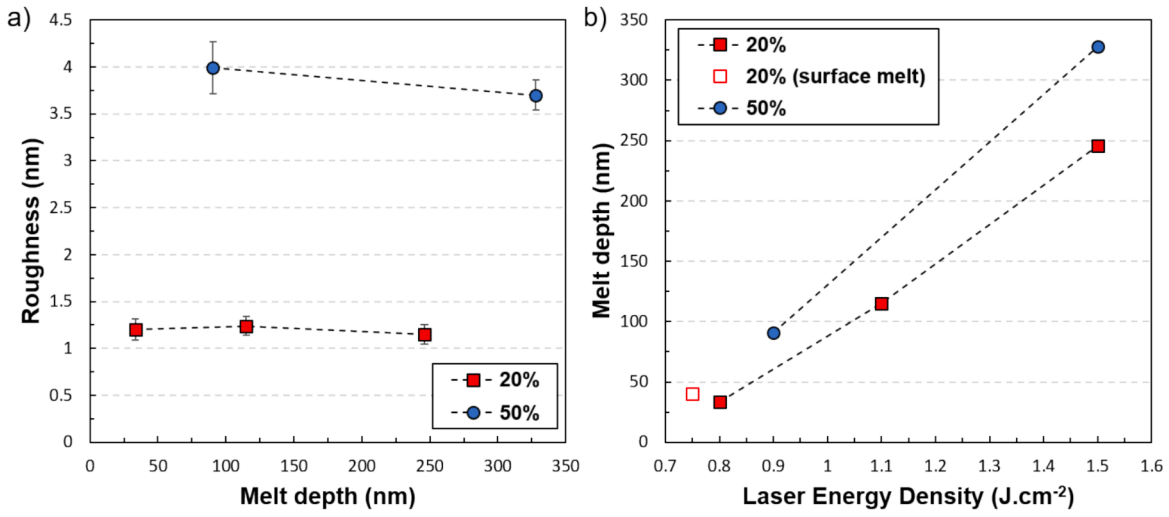

Fig. 7. (a) Evolution of the l/s interface roughness as a function of average melt depth in thick relaxed SiGe layers with 20 % or 50 % of Ge. Surface melt roughness is not shown here. (b) Evolution of the melt depth as a function of the laser energy density for r-$Si_{1-x}Ge_x$ (x = 0.2 or 0.5).

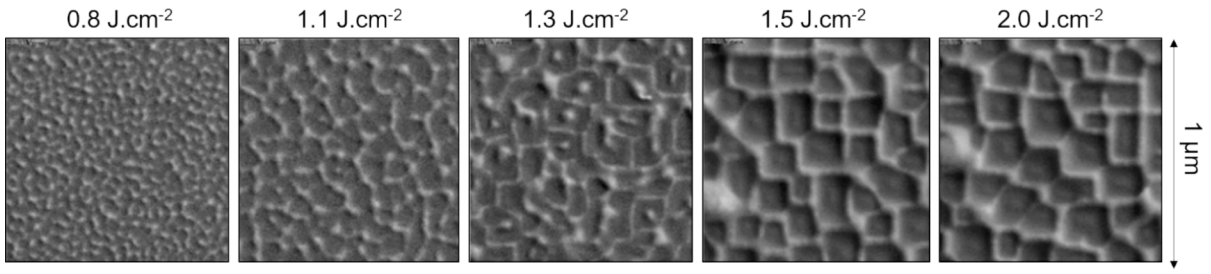

Fig. 8. 1 × 1 µm^2 top-view SEM micrographs of r-$Si_{0.8}Ge_{0.2}$ for various laser ED. Scan sides are parallel to <110> directions.

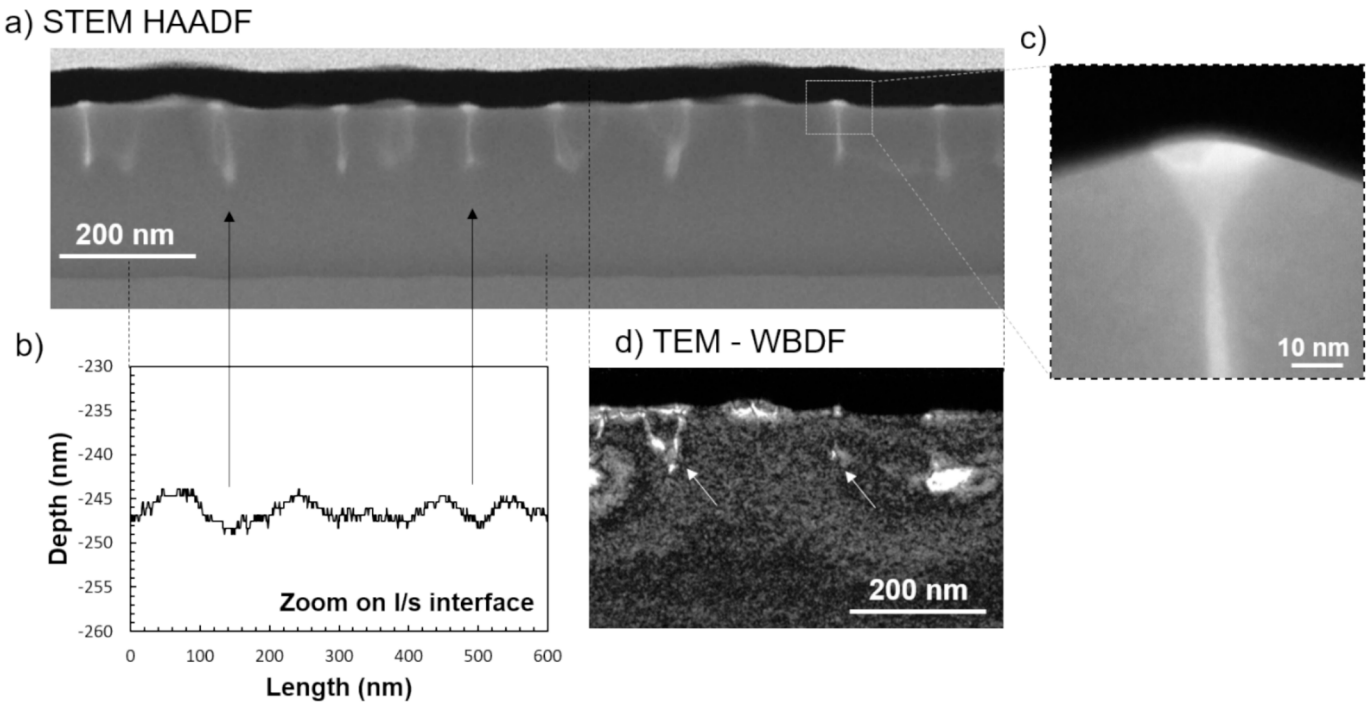

Fig. 9. (a) STEM-HAADF micrograph of a r-$Si_{0.8}Ge_{0.2}$ layer laser-annealed at 1.5 J cm^{-2}. (b) Zoom on the representative curve of the l/s interface. (c) Magnified micrograph on a Ge-rich pillar. (d) WBDF-TEM micrograph evidencing the presence of defects in the layer. The diffraction vector is g = [004].

interface is clearly rough (Fig. 7(a)). During the first steps of the melt regimes, from 0.75 to 1.1 J cm^{-2}, Ge segregates in the melted areas and the Ge composition at the layer surface continuously increases (Fig. 6 (d)). Given the wall composition estimations by EDX, such segregation may occur until pure Ge phases are locally formed. As Ge walls start to form 160 nm from the l/s interface, considering a linear evolution of the melt depth from Fig. 7(b), the cellular morphology may appear at ED between 1.2 and 1.3 J cm^{-2}. By increasing the Ge composition, layer evolution at high ED is similar but all effects are increased (segregation phenomenon, l/s interface roughness, melt depth …).

A representative curve of the l/s interface has been extracted and plotted for part of the STEM-HAADF micrograph shown in Fig. 9(b). This representation evidences that Ge-rich walls are formed at specific locations which corresponds to the valleys of the l/s interface (highlighted for two walls by black arrows). On the EDX spectra represented in Fig. 6 (d), it is evidenced that the increase of the laser ED induces a progressive increase of the Ge surface composition, because of Ge segregation, from 45 % at 0.75 J cm^{-2} to 75 % at 1.1 J cm^{-2}. In this way, assuming that the Ge segregation occurs perpendicular to the l/s interface, valleys at the l/s interface will be preferential sites for the formation of Ge-rich phases. In the stages that follow, Ge will continue to laterally segregate to form walls and the cellular surface morphology. Moreover, even if the regrowth itself of a r-$Si_{0.8}Ge_{0.2}$ layer cannot be directly observed, the presence of <110> facets between Ge-poor and Ge-rich phases near the surface (Fig. 9(c)) at the end of crystal regrowth hints at an evolution from an initially rough to a faceted l/s interface.

A TEM micrograph of r-$Si_{0.8}Ge_{0.2}$ annealed at 1.5 J cm^{-2}, taken in the WBDF mode with a diffraction vector g = [004], is shown in Fig. 9d. This micrograph evidences the presence of defects (bright contrasts) close to Ge-rich walls. These defects are generated all along the Ge-rich walls up to the r-$Si_{0.8}Ge_{0.2}$ surface. At lower ED, Ge segregation towards the surface left the layer defect-free. The l/s interface roughness remained constant regardless of the melt depth (and thus whatever of the surface structuring). This may indicate that the generation of these defects at high ED is not linked to the roughness but to the formation of the Ge-rich phase itself, leading to the formation of a cellular morphology. Similar dislocations have been observed after the regrowth of Ge implanted Si at high temperature. These so-called hairpin dislocations, due to the layer relaxation, were generated at Ge concentration maxima (higher elastic energy) and extended up to the surface [39]. Here, very similar dislocations seem to be generated due to Ge segregation. This could explain why these dislocations were found only along Ge-rich walls at high ED.

3.4. Impact of the laser pulse duration

Finally, to properly quantify the impact of nano-structuring, during the surface melt regime, on the partial and full melt regimes, investigations were performed on low-doped s-$Si_{0.7}Ge_{0.3}$:B layers with

different laser pulse durations of 25 and 146 ns, respectively. Using short pulse durations provides faster l/s interface velocity than long pulse durations. The recrystallization speed has a direct impact on the Ge concentration in the solid phase χ_S through the partition coefficient k: $\chi_S = k.\ \chi_L$ (where χ_L is the Ge concentration in the liquid phase near the l/s interface). By increasing the l/s interface velocity, the partition coefficient increases close to 1, considerably reducing Ge segregation [36,40–43]. This has been confirmed by SIMS analysis (see supporting information S3). Such observation has been recently evidenced on $Si_{1-x}Ge_x$ layers annealed by NLA with 24 ns pulses by SIMS measurements, in which Ge profile barely flat excepted at the layer surface and near to the l/s interface [44,45]. By comparison, in our previous study, using 146 ns pulses evidenced strong Ge redistribution all along the layer whatever the melting regime [15]. STEM-HAADF micrographs of low-doped s-$Si_{0.7}Ge_{0.3}$:B layers annealed in the partial (0.727 and 0.848 J cm^{-2}) and full melt (0.969 J cm^{-2}) regimes with a pulse duration of 25 ns are displayed in Fig. 10(a). The use of a shorter pulse duration during laser annealing process clearly results in a decrease of the l/s interface roughness in the partial melt regime (compared to Fig. 1(a)). Fig. 10(b) shows the evolution of the l/s roughness parameter for both pulse durations. While roughness in the full melt regime are equivalent due to the major impact of the $Si_{1-x}Ge_x$/Si interface, as highlighted in Section 3.1.1, shorter pulses induce a significant flattening of the l/s interface in the partial melt regime, with the formation of a flat interface similar to that in the full melt regime. This decrease of the l/s interface roughness seems to be beneficial to the crystalline quality of such thin layers. While stacking faults were observed with 146 ns pulse durations, no defects at all were observed, regardless of the laser ED, for 25 ns pulse durations. Once again, a significant correlation between the roughness of the l/s interface and the formation of defects in the layer was evidenced. Then, the use of shorter pulse duration during the annealing process may be beneficial to the layer properties.

4. Conclusion

In this paper, the impact of laser annealing on $Si_{1-x}Ge_x$ layers, with a focus on the liquid/solid (l/s) interface roughness, has been investigated with TEM and HR-XRD. To better understand the influence of the l/s interface roughness on the crystallinity of $Si_{1-x}Ge_x$ layers, a methodology for the quantification of this roughness based on cross-sectional STEM-HAADF micrographs has been established. This procedure enabled us to precisely understand the evolution of this roughness as a function of the $Si_{1-x}Ge_x$ layer characteristics (Ge content, doping, strain state) as well as laser annealing conditions (energy density, pulse duration). Three possible origins of the l/s interface roughness were highlighted. (i) A decrease of the initial strain state of the $Si_{1-x}Ge_x$ layer induced by B-doping led to a decrease of the roughness and a reduction of strain relaxation in the melt regimes. (ii) The Ge content had an indirect impact on interface roughness coming from self-organization during the surface melt. Higher Ge contents result in rougher interfaces. (iii) A reduction of the pulse duration used for laser annealing significantly reduced the l/s interfacial roughness. Moreover, it has been evidenced that the l/s interface roughness had a major impact on the global layer structuring under extreme conditions resulting in a cellular surface morphology with pure Ge walls. The use of B-doping and/or the use of short pulse duration may be the best options to obtain defect-free $Si_{1-x}Ge_x$ layers when using laser annealing.

CRediT authorship contribution statement

R. Demoulin: Writing – original draft, Visualization, Validation, Methodology, Investigation, Formal analysis, Data curation, Conceptualization. **R. Daubriac:** Writing – review & editing, Visualization, Validation, Project administration, Methodology, Investigation, Formal analysis. **S. Kerdilès:** Writing – review & editing, Resources, Data curation. **L. Dagault:** Resources, Formal analysis, Data curation. **O. Adami:** Resources, Investigation, Data curation. **D. Ricciarelli:** Investigation. **J.-M. Hartmann:** Writing – review & editing, Resources. **F. Chiodi:** Writing – review & editing, Resources. **A.M. Mio:** Resources, Investigation. **M. Opprecht:** Resources. **E. Scheid:** Investigation. **P. Acosta Alba:** Resources. **D. Débarre:** Resources. **A.La Magna:** Writing – review & editing, Project administration, Funding acquisition, Data curation. **F. Cristiano:** Supervision, Project administration, Funding acquisition, Conceptualization.

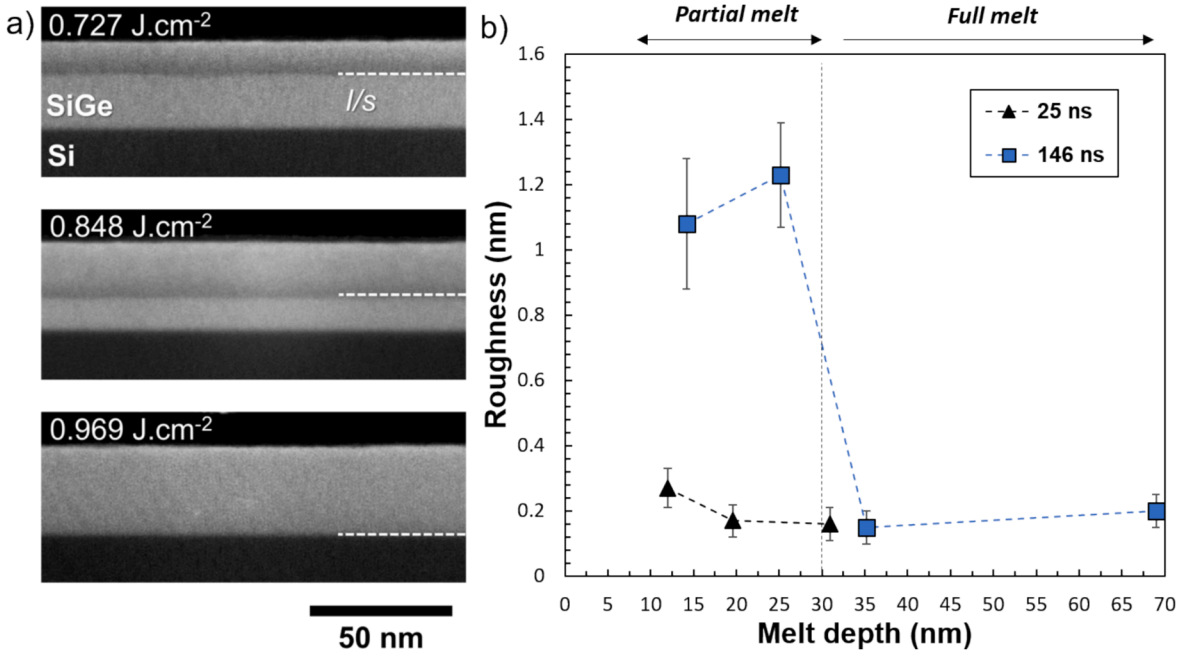

Fig. 10. (a) STEM-HAADF micrographs of low-doped s-$Si_{0.7}Ge_{0.3}$:B layers annealed with a pulse duration of 25 ns. (b) Comparison of the calculated l/s roughness parameter as a function of the melt depth for two different laser pulse durations (25 and 146 ns).

Declaration of competing interest

The authors declare that they have no known competing financial interests or personal relationships that could have appeared to influence the work reported in this paper.

Acknowledgements

Authors thank the Raimond Castaing micro-characterization platform of Toulouse for the access to TEM instruments. Authors acknowledge technical support provided by the LAAS-CNRS micro and nanotechnologies platform, member of French RENATECH network. The research leading to these results has received funding from the European Union's Horizon 2020 research and innovation programme under grant agreement No. 871813 MUNDFAB.

Appendix A. Supplementary data

Supplementary data to this article can be found online at https://doi.org/10.1016/j.apsusc.2024.161982.

Data availability

Data will be made available on request.

References

[1] T. Tabata, F. Rozé, L. Thuries, S. Halty, P.-E. Raynal, I. Karmous, K. Huet, Recent progresses and perspectives of UV laser annealing technologies for advanced CMOS devices, Electronics 11 (2022) 2636, https://doi.org/10.3390/electronics11172636.

[2] G. Fortunato, L. Mariucci, A. Pecora, V. Privitera, F. Simon, Historical evolution of pulsed laser annealing for semiconductor processing, in: Laser Annealing Process. Semicond. Technol., Elsevier, 2021, pp. 1–48, https://doi.org/10.1016/B978-0-12-820255-5.00006-4.

[3] F. Cristiano, A. La Magna, Laser Annealing Processes in Semiconductor Technology: Theory, Modeling, and Applications in Nanoelectronics, Woodhead Publishing, an imprint of Elsevier, Duxford United Kingdom, 2021.

[4] P. Acosta Alba, S. Kerdiles, B. Mathieu, R. Kachtouli, F. Mazzamuto, I. Toque-Tresonne, K. Huet, P. Besson, M. Veillerot, F. Aussenac, C. Fenouillet-Beranger, Nanosecond laser annealing for phosphorous activation in ultra-thin implanted silicon-on-insulator substrates, in: 21st Int. Conf. Ion Implant Technol, IIT IEEE, Tainan Taiwan, 2016, pp. 1–4, https://doi.org/10.1109/IIT.2016.7882896.

[5] K. Huet, J. Aubin, P.-E. Raynal, B. Curvers, A. Verstraete, B. Lespinasse, F. Mazzamuto, A. Sciuto, S.F. Lombardo, A. La Magna, P. Acosta-Alba, L. Dagault, C. Licitra, J.-M. Hartmann, S. Kerdilès, Pulsed laser annealing for advanced technology nodes: modeling and calibration, Appl. Surf. Sci. 505 (2020) 144470, https://doi.org/10.1016/j.apsusc.2019.144470.

[6] Y. Takamura, S.H. Jain, P.B. Griffin, J.D. Plummer, Thermal stability of dopants in laser annealed silicon, J. Appl. Phys. 92 (2002) 230–234, https://doi.org/10.1063/1.1481975.

[7] H. Shin, M. Lee, E. Ko, H. Ryu, S. Park, E. Kim, D.-H. Ko, Dopant activation of in situ phosphorus-doped silicon using multi-pulse nanosecond laser annealing, Phys. Status Solidi A 217 (2020) 1900988, https://doi.org/10.1002/pssa.201900988.

[8] G. Kerrien, J. Boulmer, D. Débarre, D. Bouchier, A. Grouillet, D. Lenoble, Ultra-shallow, super-doped and box-like junctions realized by laser-induced doping, Appl. Surf. Sci. 186 (2002) 45–51, https://doi.org/10.1016/S0169-4332(01)00623-7.

[9] P. Batude, L. Brunet, C. Fenouillet-Beranger, F. Andrieu, J.-P. Colinge, D. Lattard, E. Vianello, S. Thuries, O. Billoint, P. Vivet, C. Santos, B. Mathieu, B. Sklenard, C.-M.-V. Lu, J. Micout, F. Deprat, E.A. Mercado, F. Ponthenier, N. Rambal, M.-P. Samson, M. Casse, S. Hentz, J. Arcamone, G. Sicard, L. Hutin, L. Pasini, A. Ayres, O. Rozeau, R. Berthelon, F. Nemouchi, P. Rodriguez, J.-B. Pin, D. Larmagnac, A. Duboust, V. Ripoche, S. Barraud, N. Allouti, S. Barnola, C. Vizioz, J.-M. Hartmann, S. Kerdiles, P.A. Alba, S. Beaurepaire, V. Beugin, F. Fournel, P. Besson, V. Loup, R. Gassilloud, F. Martin, X. Garros, F. Mazen, B. Previtali, C. Euvrard-Colnat, V. Balan, C. Comboroure, M. Zussy, O. Mazzocchi, M.V. Faynot, in: 3D Sequential Integration: Application-Driven Technological Achievements and Guidelines, IEEE, San Francisco, CA, 2017, pp. 3.1.1–3.1.4, https://doi.org/10.1109/IEDM.2017.8268316.

[10] P. Batude, C. Fenouillet-Beranger, L. Pasini, V. Lu, F. Deprat, L. Brunet, B. Sklenard, F. Piegas-Luce, M. Casse, B. Mathieu, O. Billoint, G. Cibrario, O. Turkyilmaz, H. Sarhan, S. Thuries, L. Hutin, S. Sollier, J. Widiez, L. Hortemel, C. Tabone, M.-P. Samson, B. Previtali, N. Rambal, F. Ponthenier, J. Mazurier, R. Beneyton, M. Bidaud, E. Josse, E. Petitprez, O. Rozeau, M. Rivoire, C. Euvard-Colnat, A. Seignard, F. Fournel, L. Benaissa, P. Coudrain, P. Leduc, J.-M. Hartmann, P. Besson, S. Kerdiles, C. Bout, F. Nemouchi, A. Royer, C. Agraffeil, G. Ghibaudo, T. Signamarcheix, M. Haond, F. Clermidy, O. Faynot, M. Vinet, 3DVLSI with CoolCube process: An alternative path to scaling, in: 2015 Symp. VLSI Technol, VLSI Technol IEEE, Kyoto, Japan, 2015, pp. T48–T49, https://doi.org/10.1109/VLSIT.2015.7223698.

[11] L. Brunet, C. Fenouillet-Beranger, P. Batude, S. Beaurepaire, F. Ponthenier, N. Rambal, V. Mazzocchi, J.-B. Pin, P. Acosta-Alba, S. Kerdiles, P. Besson, H. Fontaine, T. Lardin, F. Fournel, V. Larrey, F. Mazen, V. Balan, C. Morales, C. Guerin, V. Jousseaume, X. Federspiel, D. Ney, X. Garros, A. Roman, D. Scevola, P. Perreau, F. Kouemeni-Tchouake, L. Arnaud, C. Scibetta, S. Chevalliez, F. Aussenac, J. Aubin, S. Reboh, F. Andrieu, S. Maitrejean, M. Vinet, Breakthroughs in 3D sequential technology, IEDM, IEEE, San Francisco, CA, 2018, pp. 7.2.1–7.2.4, https://doi.org/10.1109/IEDM.2018.8614653.

[12] F. Fossard, J. Boulmer, D. Débarre, J.-L. Perrossier, C. Bachelet, F. Fortuna, V. Mathet, D. Bouchier, Pseudomorphic SiGe/Si(001) layers synthesized by gas immersion laser doping, Appl. Phys. Lett. 93 (2008) 021911, https://doi.org/10.1063/1.2956674.

[13] L. Vincent, F. Fossard, T. Kociniewski, L. Largeau, N. Cherkashin, M.J. Hÿtch, D. Debarre, T. Sauvage, A. Claverie, J. Boulmer, D. Bouchier, Nanoscale concentration and strain distribution in pseudomorphic films $Si_{1-x}Ge_x$/Si processed by pulsed laser induced epitaxy, Appl. Surf. Sci. 258 (2012) 9208–9212, https://doi.org/10.1016/j.apsusc.2011.07.074.

[14] T. Kociniewski, F. Fossard, J. Boulmer, D. Bouchier, Synthesis of strained SiGe on Si (100) by pulsed laser induced epitaxy, Thin Solid Films 518 (2010) 2542–2545, https://doi.org/10.1016/j.tsf.2009.09.154.

[15] L. Dagault, S. Kerdilès, P. Acosta Alba, J.-M. Hartmann, J.-P. Barnes, P. Gergaud, E. Scheid, F. Cristiano, Investigation of recrystallization and stress relaxation in nanosecond laser annealed $Si_{1-x}Ge_x$/Si epilayers, Appl. Surf. Sci. 527 (2020) 146752, https://doi.org/10.1016/j.apsusc.2020.146752.

[16] M. Weizman, N.H. Nickel, I. Sieber, B. Yan, Laser-induced self-organization in silicon-germanium thin films, J. Appl. Phys. 103 (2008) 093536, https://doi.org/10.1063/1.2919772.

[17] J.F. Young, J.E. Sipe, H.M. van Driel, Laser-induced periodic surface structure. III. Fluence regimes, the role of feedback, and details of the induced topography in germanium, PhysRevB 30 (1984) 2001–2015, https://doi.org/10.1103/PhysRevB.30.2001.

[18] I. Karmous, F. Roze, P.-E. Raynal, K. Huet, P. Acosta Alba, T. Tabata, S. Kerdiles, Wrinkles emerging in SiO_2/Si stack during UV nanosecond laser anneal, ECSMeet. Abstr. MA2021-01 (2021) 1011, https://doi.org/10.1149/MA2021-01301011mtgabs.

[19] N.A. Sobolev, G.D. Ivlev, E.I. Gatskevich, J.P. Leitão, A. Fonseca, M.C. Carmo, A. B. Lopes, D.N. Sharaev, H. Kibbel, H. Presting, Pulsed laser annealing of Si–Ge superlattices, Mater. Sci. Eng. C 23 (2003) 19–22, https://doi.org/10.1016/S0928-4931(02)00222-9.

[20] J. Narayan, Interface instability and cell formation in ion-implanted and laser-annealed silicon, J. Appl. Phys. 52 (1981) 1289–1293, https://doi.org/10.1063/1.329753.

[21] P.I. Gaiduk, S.L. Prakopyeu, Structural Changes in SiGe/Si Layers Induced by Fast Crystallization, in: W. Skorupa, H. Schmidt (Eds.), Subsecond Annealing Adv. Mater, Springer International Publishing, Cham, 2014, pp. 79–105, https://doi.org/10.1007/978-3-319-03131-6_5.

[22] L. Dagault, P. Acosta-Alba, S. Kerdilès, J.P. Barnes, J.M. Hartmann, P. Gergaud, T. T. Nguyen, A. Grenier, A.M. Papon, N. Bernier, V. Delaye, J. Aubin, F. Cristiano, Impact of UV nanosecond laser annealing on composition and strain of undoped $Si_{0.8}Ge_{0.2}$ epitaxial layers, ECS J. Solid StateSci. Technol. 8 (2019) P202–P208, https://doi.org/10.1149/2.0191903jss.

[23] R. Gotoh, K. Fujiwara, X. Yang, H. Koizumi, J. Nozawa, S. Uda, Formation mechanism of cellular structures during unidirectional growth of binary semiconductor Si-rich SiGe materials, Appl. Phys. Lett. 100 (2012) 021903, https://doi.org/10.1063/1.3675860.

[24] G. Taraschi, A.J. Pitera, L.M. McGill, Z.-Y. Cheng, M.L. Lee, T.A. Langdo, E. A. Fitzgerald, Ultrathin strained Si-on-Insulator and SiGe-on-insulator created using low temperature wafer bonding and metastable stop layers, J. Electrochem. Soc. 151 (2004) G47, https://doi.org/10.1149/1.1629101.

[25] C.Y. Ong, K.L. Pey, X. Li, X.C. Wang, C.M. Ng, L. Chan, Laser annealing induced high Ge concentration epitaxial SiGe layer in $Si_{1-x}Ge_x$ virtual substrate, Appl. Phys. Lett. 93 (2008) 041112, https://doi.org/10.1063/1.2962991.

[26] A. Rodríguez, T. Rodríguez, A. Sanz-Hervás, A. Kling, J.C. Soares, M.F. da Silva, C. Ballesteros, R.M. Gwilliam, Strain compensation by heavy boron doping in $Si_{1-x}Ge_x$ layers grown by solid phase epitaxy, J. Mater. Res. 12 (1997) 1698–1705, https://doi.org/10.1557/JMR.1997.0234.

[27] G. Bisognin, D. De Salvador, E. Napolitani, M. Berti, A. Carnera, S. Mirabella, L. Romano, M.G. Grimaldi, F. Priolo, Substitutional B in Si: accurate lattice parameter determination, J. Appl. Phys. 101 (2007) 093523, https://doi.org/10.1063/1.2720186.

[28] D. Ricciarelli, G. Mannino, I. Deretzis, G. Calogero, G. Fisicaro, R. Daubriac, F. Cristiano, R. Demoulin, P.P. Michałowski, P. Acosta-Alba, J.-M. Hartmann, S. Kerdilès, A. La Magna, Impact of surface reflectivity on the ultra-fast laser melting of silicon-germanium alloys, Mater. Sci. Semicond. Process. 165 (2023) 107635, https://doi.org/10.1016/j.mssp.2023.107635.

[29] X. Li, K. Maute, M.L. Dunn, R. Yang, Strain effects on the thermal conductivity of nanostructures, Phys. Rev. B 81 (2010) 245318, https://doi.org/10.1103/PhysRevB.81.245318.

[30] Z. Yang, R. Feng, F. Su, D. Hu, X. Ma, Isotope and strain effects on thermal conductivity of silicon thin film, Phys. E Low-Dimens. Syst. Nanostructures 64 (2014) 204–210, https://doi.org/10.1016/j.physe.2014.07.026.

[31] K.D. Parrish, A. Jain, J.M. Larkin, W.A. Saidi, A.J.H. McGaughey, Origins of thermal conductivity changes in strained crystals, Phys. Rev. B 90 (2014) 235201, https://doi.org/10.1103/PhysRevB.90.235201.
[32] R. Cheaito, J.C. Duda, T.E. Beechem, K. Hattar, J.F. Ihlefeld, D.L. Medlin, M. A. Rodriguez, M.J. Campion, E.S. Piekos, P.E. Hopkins, Experimental investigation of size effects on the thermal conductivity of silicon-germanium alloy thin films, Phys. Rev. Lett. 109 (2012) 195901, https://doi.org/10.1103/PhysRevLett.109.195901.
[33] M. Asheghi, K. Kurabayashi, R. Kasnavi, K.E. Goodson, Thermal conduction in doped single-crystal silicon films, J. Appl. Phys. 91 (2002) 5079–5088, https://doi.org/10.1063/1.1458057.
[34] G.A. Slack, Thermal conductivity of pure and impure silicon, silicon carbide, and diamond, J. Appl. Phys. 35 (1964) 3460–3466, https://doi.org/10.1063/1.1713251.
[35] J.A. Carruthers, T.H. Geballe, H.M. Rosenberg, J.M. Ziman, The thermal conductivity of germanium and silicon between 2 and 300° K, Proc. R. Soc. Lond. Ser. Math. Phys. Sci. 238 (1957) 502–514, https://doi.org/10.1098/rspa.1957.0014.
[36] T. Tabata, J. Aubin, K. Huet, F. Mazzamuto, Segregation and activation of Ga in high Ge content SiGe by UV melt laser anneal, J. Appl. Phys. 125 (2019) 215702, https://doi.org/10.1063/1.5096889.
[37] G.D. Ivlev, N.M. Kazuchits, S.L. Prakopyeu, M.S. Rusetsky, P.I. Gaiduk, The structure and photoconductivity of SiGe/Si epitaxial layers modified by single-pulse laser radiation, Tech. Phys. Lett. 40 (2014) 1042–1044, https://doi.org/10.1134/S1063785014120104.
[38] X. Yang, K. Fujiwara, N.V. Abrosimov, R. Gotoh, J. Nozawa, H. Koizumi, A. Kwasniewski, S. Uda, The critical growth velocity for planar-to-faceted interfaces transformation in SiGe crystals, Appl. Phys. Lett. 100 (2012) 141601, https://doi.org/10.1063/1.3698336.
[39] F. Cristiano, A. Nejim, Y. Suprun-Belevich, A. Claverie, P.L.F. Hemment, Formation of extended defects and strain relaxation in ion beam synthesised SiGe alloys, Nucl. Instrum. Methods Phys. Res. Sect. B Beam Interact. Mater. At. 147 (1999) 35–42, https://doi.org/10.1016/S0168-583X(98)00589-8.
[40] D.P. Brunco, M.O. Thompson, D.E. Hoglund, M.J. Aziz, H.-J. Gossmann, Germanium partitioning in silicon during rapid solidification, J. Appl. Phys. 78 (1995) 1575–1582, https://doi.org/10.1063/1.360251.
[41] G. Calogero, D. Raciti, D. Ricciarelli, P. Acosta-Alba, F. Cristiano, R. Daubriac, R. Demoulin, I. Deretzis, G. Fisicaro, J.-M. Hartmann, S. Kerdilès, A. La Magna, Atomistic insights into ultrafast SiGe nanoprocessing, J. Phys. Chem. C 127 (2023) 19867–19877, https://doi.org/10.1021/acs.jpcc.3c05999.
[42] G.V. Luong, S. Wirths, S. Stefanov, B. Holländer, J. Schubert, J.C. Conde, T. Stoica, U. Breuer, S. Chiussi, M. Goryll, D. Buca, S. Mantl, Study of dopant activation in biaxially compressively strained SiGe layers using excimer laser annealing, J. Appl. Phys. 113 (2013) 204902, https://doi.org/10.1063/1.4807001.
[43] T. Tabata, B. Curvers, K. Huet, S.A. Chew, J.-L. Everaert, N. Horiguchi, 3D simulation for melt laser anneal integration in FinFET's contact, IEEE J. Electron Devices Soc. 8 (2020) 1323–1327, https://doi.org/10.1109/JEDS.2020.3030923.
[44] K. Lee, C. Jo, D. Yoon, S. Baik, D.-H. Ko, Evaluation of the chemical states and electrical activation of ultra-highly B-doped Si1-xGex by ion implantation and subsequent nanosecond laser annealing, Appl. Surf. Sci. 657 (2024) 159756, https://doi.org/10.1016/j.apsusc.2024.159756.
[45] C. Jo, K. Lee, D. Yoon, D.-H. Ko, Strain behavior and dopant activation of heavily in-situ B-doped SiGe epitaxial films treated by nanosecond laser annealing, Mater. Sci. Semicond. Process. 175 (2024) 108215, https://doi.org/10.1016/j.mssp.2024.108215.